Chinese Journal of Aeronautics, (2014),27(6): 1586–1597

Chinese Society of Aeronautics and Astronautics
& Beihang University

Chinese Journal of Aeronautics

cja@buaa.edu.cn
www.sciencedirect.com

Damage characteristics and constitutive modeling of the 2D C/SiC composite: Part I – Experiment and analysis

Li Jun, Jiao Guiqiong *, Wang Bo, Yang Chengpeng, Wang Gang

Department of Engineering Mechanics, Northwestern Polytechnical University, Xi'an 710129, China

Received 25 December 2013; revised 8 February 2014; accepted 7 March 2014
Available online 22 October 2014

KEYWORDS

Ceramic matrix composites;
Damage;
Inelastic strain;
Mechanical testing;
Strength

Abstract This paper reports an experimental investigation on the macroscopic mechanical behaviors and damage mechanisms of the plain-woven (2D) C/SiC composite under in-plane on- and off-axis loading conditions. Specimens with 15°, 30°, and 45° off-axis angles were prepared and tested under monotonic and incremental cyclic tension and compression loads. The obtained results were compared with those of uniaxial tension, compression, and shear specimens. The relationships between the damage modes and the stress state were analyzed based on scanning electronic microscopy (SEM) observations and acoustic emission (AE) data. The test results reveal the remarkable axial anisotropy and unilateral behavior of the material. The off-axis tension test results show that the material is fiber-dominant and the evolution rate of damage and inelastic strain is accelerated under the corresponding combined biaxial tension and shear loads. Due to the damage impediment effect of compression stress, compression specimens show higher mechanical properties and lower damage evolution rates than tension specimens with the same off-axis angle. Under cyclic tension–compression loadings, both on-axis and off-axis specimens exhibit progressive damage deactivation behaviors in the compression range, but with different deactivation rates.

1. Introduction

As a typical ceramic matrix composite, the continuous carbon fiber reinforced silicon carbide (C/SiC) composite exhibits excellent oxidation resistance properties, endurance to very high temperature, and good toughness to prevent catastrophic failure under mechanical loadings.[1] Because of these properties, this material has a promising future for thermo-structural applications in aeronautic engines, gas turbines, detonation engines, thermal protection systems of reusable launch vehicles, and so on.[1–3] Therefore, it becomes important to extensively investigate its mechanical behaviors under different loading conditions and further develop an appropriate macroscopic constitutive model for its structural design.

In a chemical vapor infiltration (CVI) processed C/SiC composite, although the theoretical tensile modulus of the

* Corresponding author. Tel.: +86 29 88431023.
E-mail address: jiaogq@nwpu.edu.cn (G. Jiao).

Peer review under responsibility of Editorial Committee of CJA.

ELSEVIER Production and hosting by Elsevier

http://dx.doi.org/10.1016/j.cja.2014.10.026

SiC matrix is higher than that of the carbon fiber,[4] its load-bearing capability is weakened by the residual porosity formed in the fabrication process and the initial microcracks induced by the relief of thermal residual stress which is generated due to the mismatch between coefficients of thermal expansion of the fiber and the matrix.[4,5] For this reason, Morscher et al. classified this material as a "fiber-dominated" composite.[6] During last two decades, much work has been done regarding the mechanical behaviors and internal damage mechanisms of the C/SiC composite under uniaxial tension,[4,7–9] compression,[10] in-plane and interlaminar shear loads,[11–13] with the help of traditional strain measurements, SEM observation,[7] ultrasonic methods,[14–16] and an AE approach.[17] It has been well-known that this material shows remarkable non-linear stress/strain behaviors under on-axis tension and shear loads due to multiple energy dissipation mechanisms including matrix cracking, interface debonding and sliding, fiber breakage and pull-out, delamination, and so on[4,18]; it usually depicts approximately linear elastic response until rupture under uniaxial compression.[4,10] Besides, the incremental loading–unloading–reloading (cyclic) test method provides an effective way to determine the damage state, inelastic strain, and even the thermal residual stress of the material, so it has been widely used in the field of ceramic matrix composites.[19] During the cyclic tension or shear loading, the C/SiC composite develops stress/strain hysteresis loops due to the frictional sliding between the fiber and the matrix in the interface deboned region. This hysteresis behavior was studied by Li[20] through experiments and micro-mechanics approaches. Although the basic mechanical behaviors of the C/SiC composite have been well documented, according to our knowledge, quite few studies have been published regarding the mechanical responses of the C/SiC material under proportional, biaxial, or triaxial loadings. Off-axis tension, compression, and tension–compression tests performed on 2D and 3D C/SiC composites were respectively reported by Chaboche et al.[21] and Marcin et al.,[22] but the related results were mainly used for validation of the proposed macroscopic constitutive model, and the damage mechanisms of these materials were not discussed in detail.

The present paper aims to obtain a better understanding of the in-plane mechanical behaviors especially the damage characteristic of the 2D C/SiC composite under combined biaxial tension/compression and shear loadings. For this reason, specimens with various off-axis angles were tested under in-plane tension, compression, and tension–compression loads, and then their global and local stress/strain relationships, mechanical properties, and evolution laws of damage and inelastic strain were compared. Damage and its deactivation mechanisms under these loading conditions were analyzed based on SEM observations and AE data.

2. Experiment

2.1. Specimens preparation

2D C/SiC composite specimens studied in this paper were prepared by CVI technology. The preforms were laminated by T300 carbon fiber plain-woven fabrics, and then the CVI process was employed to deposit a thin layer of pyrocarbon interface and a SiC matrix at around 1000 °C. The detailed fabrication procedure can be found in Ref. [23] The prepared panel was then sliced into straight-sided specimens with different off-axis angles (θ = 0°, 15°, 30° or 45°) and on-axis Iosipescu ones, as illustrated in Figs. 1 and 2, respectively. After final deposition of the ~50 μm SiC matrix on the surface, the bulk density of the as-received specimens is about 2.0 g/cm^3, with fiber and porosity contents of 40% and 10–15%, respectively.

2.2. Tension and compression tests

Tests performed on the straight-sided specimens shown in Fig. 1 can be divided into tension and compression types, and their dimensions and test methods are referred to ASTM standards designated C1275-00 and C1358-05, respectively. Strain gage rosettes, designated as SG1 and SG2 in Fig. 1, were mounted on the gage section of the straight-sided specimens. In order to provide a compliant layer for gripping, aluminum tabs with an oblique angle were stuck on two shoulders of the specimens using epoxy adhesive. A shorter length of gage section L_g was adjusted for the compression and cyclic tension–compression specimens to prevent buckling failure modes.

Two oriented strain gage rosettes were centrally mounted on the off-axis specimens (see Fig. 1) to measure the normal strains ε_1 and ε_2 along the fiber directions in the material coordinate system (MCS) and ε_x and ε_y in the longitudinal and lateral directions in the global coordinate system (GCS). In the case of plane stress state, there are strain transformation formulae[24]

$$\begin{bmatrix} \varepsilon_1 \\ \varepsilon_2 \\ \gamma_{12} \end{bmatrix} = \begin{bmatrix} m^2 & n^2 & mn \\ n^2 & m^2 & -mn \\ -2mn & 2mn & m^2-n^2 \end{bmatrix} \begin{bmatrix} \varepsilon_x \\ \varepsilon_y \\ \gamma_{xy} \end{bmatrix} \tag{1}$$

where $m = \cos\theta$, $n = \sin\theta$; γ_{12} and γ_{xy} are engineering shear strain components, which can be determined in the formulae.

The in-plane normal and shear stresses (σ_1, σ_2, and τ_{12}) in the MCS developed within the specimens in the absence of end constraint are given as follows[25]

$$\begin{cases} \sigma_1 = m^2\sigma_x \\ \sigma_2 = n^2\sigma_x \\ \tau_{12} = -mn\sigma_x \end{cases} \tag{2}$$

where σ_x is the longitudinal tension or compression stress.

Since the load and strain data were simultaneously recorded during the tests, the macroscopic stress/strain curves (σ_x/ε_x or ε_y, σ_1/ε_1, σ_2/ε_2, τ_{12}/γ_{12}) in both the GCS and the MCS can be obtained from the above analysis. Besides, one can deduce from Eq. (2) that, except the on-axis specimens (θ = 0°), the woven fabrics in the off-axis specimens are under combined biaxial tension (or compression) and shear stress states in the MCS during longitudinal tension (or compression) loading, respectively.

In addition to the monotonic loading tests, an incremental cyclic test method was applied to collect the information of stiffness degradation and inelastic strain of the material at different stress levels. Except the 0° compression specimens, incremental cyclic tension and compression tests were carried out on these straight-sided specimens, and tension–compression tests were performed on the 0° on-axis, 30° and 45° off-axis specimens to study possible damage-deactivation behaviors. All these tests were conducted on servo-hydraulic

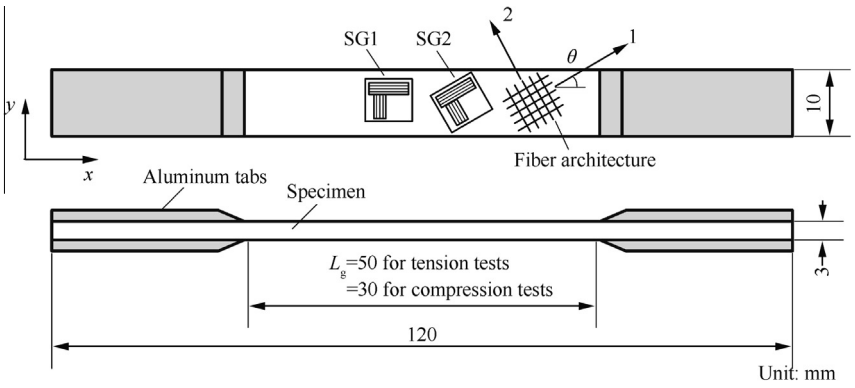

Fig. 1 A schematic of the tension/compression specimen.

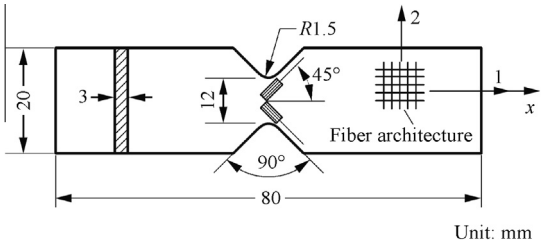

Fig. 2 A schematic of the 0° Iosipescu specimens with ±45° strain gages.

testing machines. In order to promote the accuracy of force measurements, a testing machine with a 50-kN full-scale load cell (Model 8801, Instron Ltd., England) for the 0° compression specimens and one with a 10-kN full-scale load cell (Model 8871, Instron Ltd., England) for other tests were selected. The force-controlled testing mode with a fixed rate of 6 kN/min for loading and unloading blocks was applied.

2.3. Shear test

The shear test was carried out on the 0° Iosipescu specimens (see Fig. 2) using a four-point asymmetric flexure fixture and an electronic mechanical testing machine (Model DNS100, Cimach Ltd., China), and the test method was referred to ASTM standard C1292-05. Monotonic and incremental cyclic tests with a fixed force rate of 1.5 kN/min were successively conducted. The engineering shear strain γ_{12} is equal to the summation of absolute values of the normal strains measured by two gage elements mounted at ±45° to the loading axis (i.e., $\gamma_{12} = |\varepsilon_{+45^\circ}| + |\varepsilon_{-45^\circ}|$). Back-to-back strain gages were used to monitor and correct a possible twisting effect on the test results.

All the above tests were carried out at room temperature, and at least four valid results were obtained for the basic on-axis tests and two for each type of the off-axis tests. Acoustic emission (AE) activities of some tension and compression specimens were recorded using a data acquisition system (PCI-2, Physical Acoustic Corp., USA). The AE signals were monitored by a single resonant transducer attached in the specimen's gage section and the pre-amplifier was set at 40 dB. After the mechanical tests, the damage modes on the fractured surfaces of the tested specimens were examined by SEM (JSM-6390, JEOL Ltd., Japan).

3. Results and discussion

3.1. Tension and shear behaviors

The typical monotonic and incremental cyclic tension stress/strain curves of the 0° on-axis and 15°, 30°, and 45° off-axis specimens in the GCS and the shear stress/strain relationships of the 0° Iosipescu specimens are respectively shown in Figs. 3 and 4, where L and T denote longitudinal and transverse strains, respectively. It can be seen that all of these tension and shear specimens exhibit remarkable non-linear stress/strain relationships due to the progressive stiffness degradation and accumulation of inelastic strain. The monotonic stress/strain curves approximately envelop the incremental cyclic ones, which indicates that no apparent additional damage occurs during the unloading–reloading process. Different from the transverse response of the 0° tension specimens, the transverse strain of the off-axis tension specimens keeps negative up to failure, and the 45° off-axis tension specimens have the highest initial Poisson's ratio.

The mechanical properties of the tension, compression, and 0° Iosipescu shear specimens are summarized in Table 1, where E^0, v, σ_0, σ_u, and ε_f denote the initial elastic modulus, Poisson's ratio, proportional limit stress, ultimate strength, and (engineering) fracture strain, respectively. It can be found that the tension specimens with larger θ have a tendency to show lower longitudinal tension modulus, proportional limit, and strength, but their fracture strain tends to be higher. These results reveal the axial anisotropy of the tensile mechanical behavior, and further prove that the material belongs to fiber-dominant composites.

The normal and shear stress/train relationships (σ_1/ε_1, σ_2/ε_2, $|\tau_{12}|/|\gamma_{12}|$) in the MCS of these off-axis specimens were also obtained through analysis as discussed in Section 2.2, and the typical results are presented in Fig. 5. It can be seen that these local stress/strain curves show similar non-linear characteristics of the global responses depicted in Fig. 3. However, when compared with the on-axis tension and shear behaviors of the material (see Figs. 3 and 4), these curves exhibit a lower elastic domain and a faster development rate of modulus degradation and inelastic strain as the corresponding stress components increase. This phenomenon is especially true in Fig. 5(b), since noticeable damage and inelastic strain can be detected at a very low stress level.

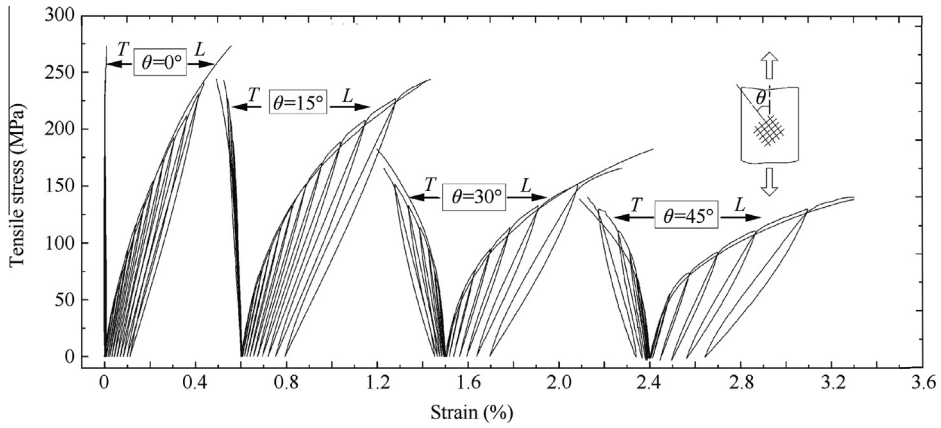

Fig. 3 Typical stress/strain curves in the GCS of the straight-sided specimens with different off-axis angles (θ) under monotonic and incremental cyclic tension loadings.

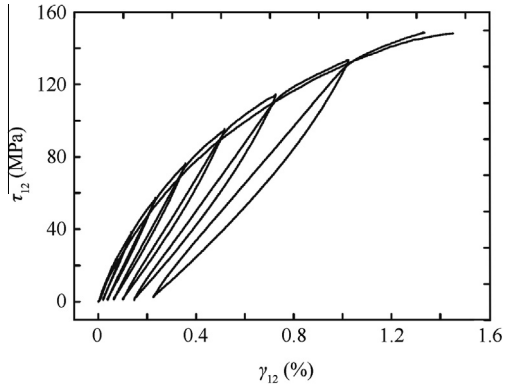

Fig. 4 Typical monotonic and cyclic shear stress/strain curves of the 0° Iosipescu specimens.

In order to quantitatively analyze the damage characteristic of the material, the degradation ratio of the unloading modulus E^{d} to the initial elastic modulus E^0 is selected as a measure of damage state according to the characteristics of the cyclic tension and shear stress/strain curves, as illustrated in Fig. 6, where the hysteresis effect is not considered in present study. Accordingly, we introduce three scalar damage variables d_i (i = 1, 2, 6) on the principle axes of the material

$$\begin{cases} d_1 = 1 - \dfrac{E_1^{\mathrm{d}}}{E_1^0} \\ d_2 = 1 - \dfrac{E_2^{\mathrm{d}}}{E_2^0} \\ d_6 = 1 - \dfrac{G_{12}^{\mathrm{d}}}{G_{12}^0} \end{cases} \tag{3}$$

where E_1, E_2, and G_{12} are engineering elastic constants; superscripts "0" and "d" respectively denote the initial and damaged states of the material.

Meanwhile, the strain ε is divided into two parts

$$\varepsilon = \varepsilon^{\mathrm{e}} + \varepsilon^{\mathrm{p}} \tag{4}$$

where ε^{e} and ε^{p} denote the elastic and inelastic strains, respectively.

Thus we obtain the evolution laws of damage variables and inelastic strain (see Figs. 7 and 8, respectively) in the MCS of the tension and shear specimens based on the test results. Note that the evolution laws of d_2/σ_2 and d_1/σ_1 are the same for the 0° and 45° off-axis tension specimens because of their symmetric mechanical properties. As the corresponding stress components σ_1, σ_2, and τ_{12} increase, Fig. 7 shows that the damage variables d_1, d_2, and d_6 of the off-axis tension specimens develop at faster rates than those of the on-axis tension and shear specimens. Specimens with larger θ exhibit higher development rates of the damage variable d_1 versus the stress component σ_1 and an increasing tendency in their ultimate damage values (see Fig. 7(a)). Comparatively, Fig. 7(b) indicates that the tensile moduli of the 15° and 30° off-axis specimens degrade rapidly, although the material along this fiber direction is subjected to a low level of the tension stress σ_2. In addition, the shear damage variable d_6 of the off-axis tension specimens develops faster than that of on-axis ones (see Fig. 7(c)); however, the differences among these off-axis specimens are not very obvious.

Fig. 8 shows that the inelastic strain of the off-axis tension specimens in the MCS accumulates still faster than that of the on-axis tension and shear specimens, and the differences among these specimens are similar to the observations in Fig. 7. These results are reasonable because the formation of inelastic strain is mainly attributed to the irreversible interface sliding between the fiber and the matrix and the release/redistribution of axial thermal residual stress,[4,18] which are related to the damage mechanisms of interface debonding and matrix microcracking. That is to say, a faster damage evolution rate results in a faster accumulation rate of inelastic strain.

The SEM micrographs in Figs. 9 and 10 reveal most of the damage and failure modes generated in the tension and Iosipescu specimens, respectively. Fig. 9(a) shows the typical tensile damage modes of the 0° tension specimens including transverse matrix cracks, interface debonding, fiber breakage and pull-out; meanwhile, Fig. 10 reveals that interface debonding, 45° oriented matrix microcracks, and fiber breakage are major shear damage and fracture modes of the material. Similar to the damage modes of the 0° tension specimens, matrix cracks are densely distributed in the fracture surfaces of the 15° off-axis tension specimens (Fig. 9(b)), most of which are vertical to the fiber and the rest are nearly perpendicular to the global loading direction. Comparatively, the matrix microcracks vertical to the fiber can also be found in the 30° and 45° off-axis tension specimens (Fig. 9(c) and (d)), however, their damage

Table 1 Mechanical properties of 2D C/SiC specimens with different off-axis angles (θ).

Test mode	θ (°)	E^0 (GPa)	v	σ_0 (MPa)	σ_u (MPa)	ε_f (%)
Tension	0	142.06 ± 13.69	0.07 ± 0.02	19.53 ± 1.07	265.28 ± 15.95	0.50 ± 0.07
	15	121.74 ± 3.10	0.17 ± 0.03	12.71 ± 7.48	199.22 ± 52.43	0.55 ± 0.33
	30	106.04 ± 10.18	0.30 ± 0.03	7.70 ± 1.46	173.96 ± 8.88	0.80 ± 0.11
	45	102.05 ± 18.35	0.34 ± 0.02	7.36 ± 2.94	125.08 ± 11.81	0.70 ± 0.18
Compression	0	144.87 ± 1.35	0.06 ± 0.01	158.28 ± 14.37	338.94 ± 11.51	0.23 ± 0.01
	15	127.58 ± 2.03	0.14 ± 0.01	127.32 ± 13.99	299.86 ± 16.84	0.23 ± 0.01
	30	104.12 ± 12.80	0.35 ± 0.03	27.43 ± 6.91	279.32 ± 3.06	0.38 ± 0.04
	45	99.89 ± 14.26	0.36 ± 0.03	21.80 ± 2.09	257.84 ± 16.40	0.44 ± 0.07
Shear	0	37.34 ± 5.53		12.96 ± 3.73	139.76 ± 16.71	1.40 ± 0.20

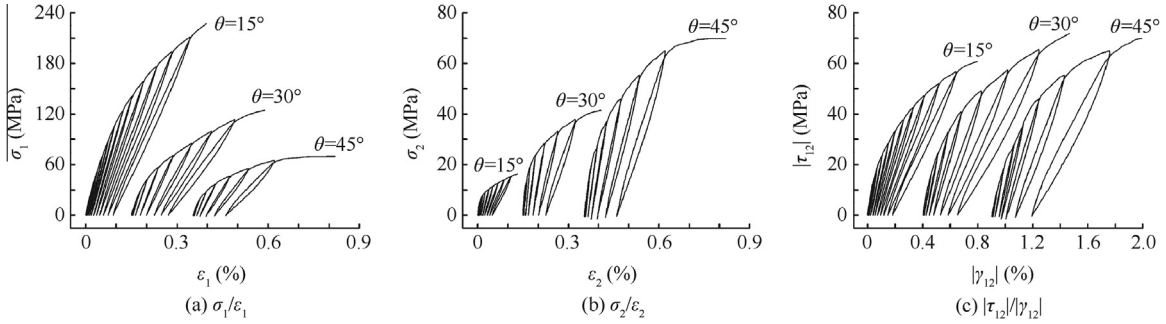

Fig. 5 Typical incremental cyclic stress/strain curves in the MCS of the off-axis tension specimens.

and fracture modes convert to coupled tensile and shear ones because more fibers are exposed and the matrix surrounding the fiber bundles is left due to interface debonding.

Fig. 11 shows the typical AE and strain data of the 0° on-axis and 45° off-axis specimens during the incremental cyclic tension tests. Fig. 11(a) reveals that AE activity is very intense in the on-axis tension specimen, and signals can be detected at a stress level well below the proportional limit stress. The AE activity in the early stage of the tension tests is probably caused by an array of non-interacting microcracks[26] which are able to relieve the thermal residual stress without affecting the elastic modulus of the material. As the stress increases constantly in the sequent loading blocks, more AE counts are recorded and the accumulated AE energy increases rapidly. In this stage, the damage mechanisms such as matrix microcracking, interface debonding, fiber breakage and delamination are considered to be the main AE sources[27] and consequently they lead to the strain nonlinearity. The increasing rate of accumulated AE energy slows down near the failure of the specimen, and fiber rupture and pull-out as well as the propagation of the fracture plane produce significant AE counts and energy when the applied load reaches the ultimate strength. Comparatively, Fig. 11(b) shows that the AE activity of the 45° off-axis specimen during tension loading is also observable, but its AE counts is much less and the maximum accumulated AE energy is about 1/10 of that recorded in the 0° on-axis specimen. This comparison result is consistent with the SEM observations that more interface debonding occurred in the 45° off-axis specimen (Fig. 9(d)), which is thought to be the AE source with the lowest energy level for the composite with weak interfaces.[28] During the cyclic loadings, AE counts and energy increase are negligible until the stress (or strain) exceeds the maximum

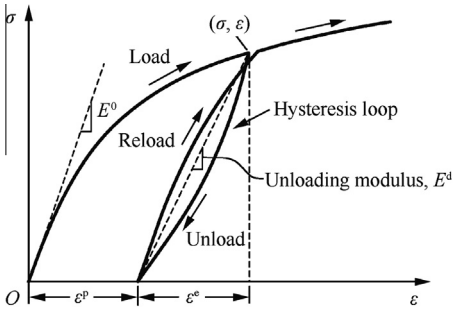

Fig. 6 A schematic of quantitative analysis of the incremental cyclic tension or shear stress/strain curve.

stress (or strain) in the previous cycle. This phenomenon reveals the distinct "Kaiser effect"[29] of the material and it also indicates that re-opening of the matrix microcracks and interface sliding do not create significant AE.

The SEM observations and AE data prove that the damage and fracture modes of the off-axis tension specimens were resulted from a combined effect of biaxial tension and shear stress. Besides, the matrix microcracks in the fiber bundles can be mainly divided into two groups: (i) microcracks perpendicular to the longitudinal loading direction, which are related to the isotropic microcracking of the SiC matrix; (ii) microcracks vertical to the reinforcing fiber, which were probably caused by the superimposition of the external tension stress and the axial tensile thermal residual stress existed in the as-processed matrix. The latter group belongs to orthotropic damage and can be more frequently found in these tension

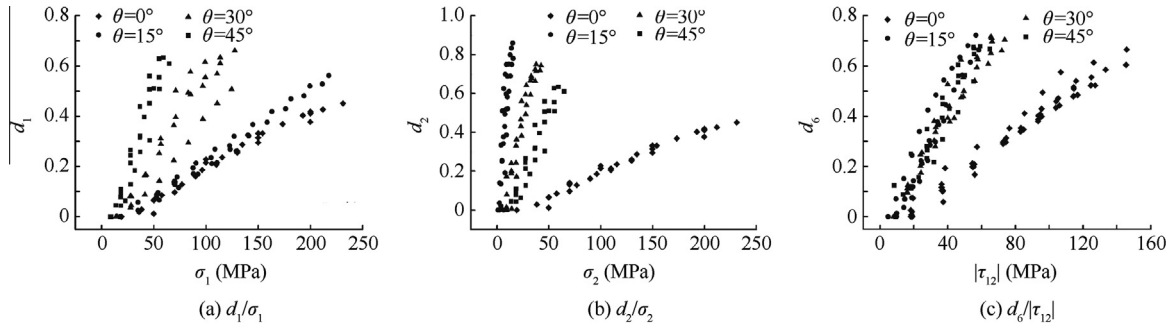

Fig. 7 Evolution laws of damage variables in the MCS of the tension and shear specimens with different off-axis angles (θ).

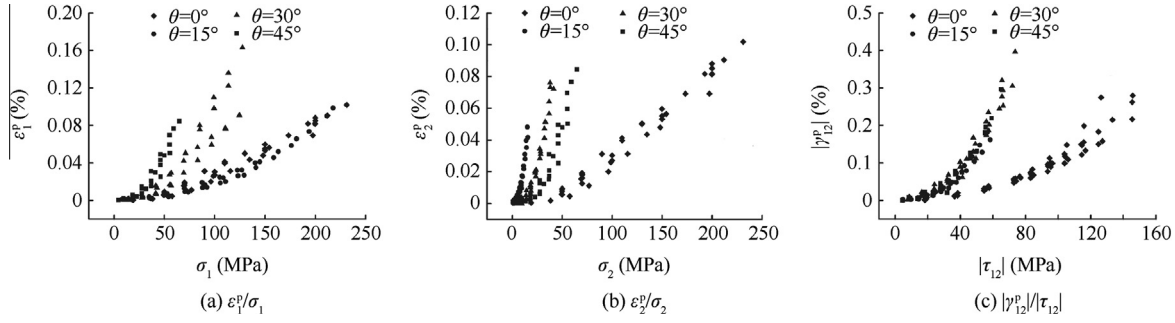

Fig. 8 Evolution laws of inelastic strain in the MCS of the tension and shear specimens with different off-axis angles (θ).

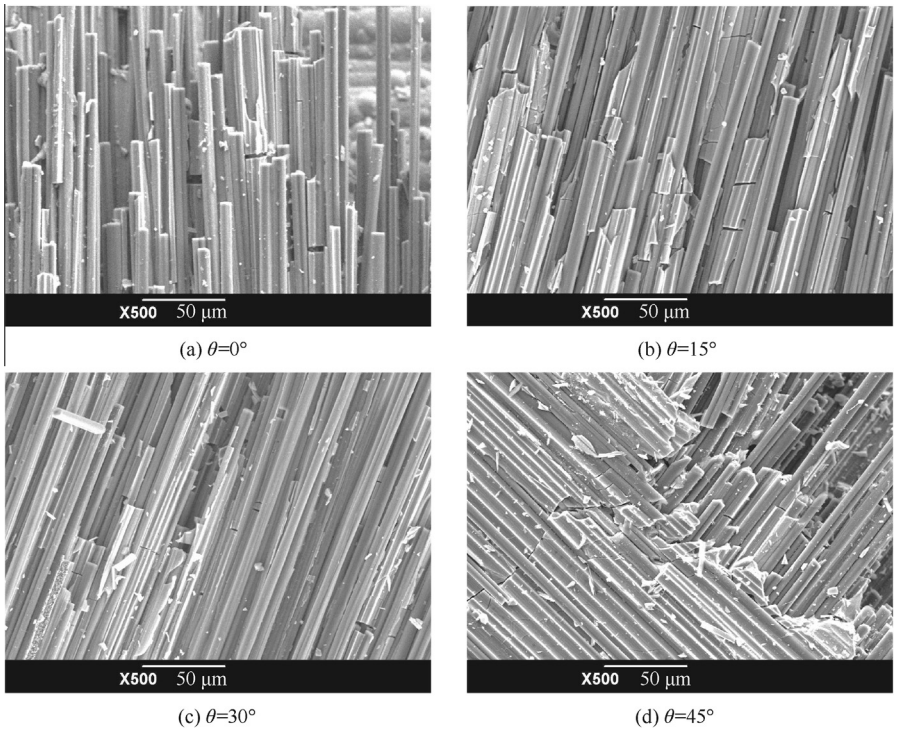

Fig. 9 SEM observations on fracture surfaces of the tension specimens with different off-axis angles (θ) (the loading direction is approximately vertical).

specimens. Moreover, the interface debonding flaws are naturally parallel to the fibers. As a result, we can conclude that the microscopic damage is mainly orthotropic in the material under tension and/or shear loads.

Additionally, the coupling effect among various damage modes should not be neglected. Firstly, biaxial tension loads resulted in more loosened woven fiber bundles by bringing more matrix microcracks and interface debonding flaws than

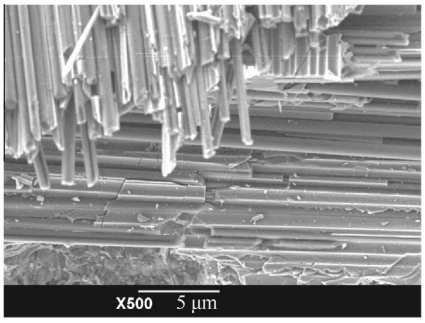

Fig. 10 SEM micrograph showing the fracture surface of a 0° Iosipescu shear specimen.

the uniaxial tension case, which would simultaneously impair the shear load-bearing capacity of the material; secondly, the shear stress generated matrix cracks and interface debonding in the material, which would reduce the load-bearing and load-transfer capacities of the matrix and the interface respectively and in turn accelerate the development of tensile damage variables. In a word, damage coupling under combined biaxial tension and shear loads should be the reason for the accelerated damage evolution process found in Fig. 7.

3.2. Compression behavior

The stress/strain curves in the GCS of the 0°, 15°, 30°, and 45° off-axis specimens under monotonic and incremental cyclic compression loadings are shown in Fig. 12, from which one can notice that the 0° and 15° off-axis specimens exhibit nearly elastic compression stress/strain relationships, with only slight stiffness degradation close to fracture; meanwhile, no apparent residual strain can be detected and their global Poisson's ratio v_{xy} nearly keeps constant. Comparatively, the 30° and 45° off-axis specimens show apparent non-linear mechanical responses because of progressive stiffness degradation and accumulation of inelastic strain. The mechanical properties of these compression specimens are summarized in Table 1.

In comparison with the mechanical responses of the tension specimens shown in Fig. 4 and Table 1, the compression specimens, on one hand, show similar downtrend in the averaged mechanical properties including the compressive modulus, proportional limit, and ultimate strength, as well as an inverse

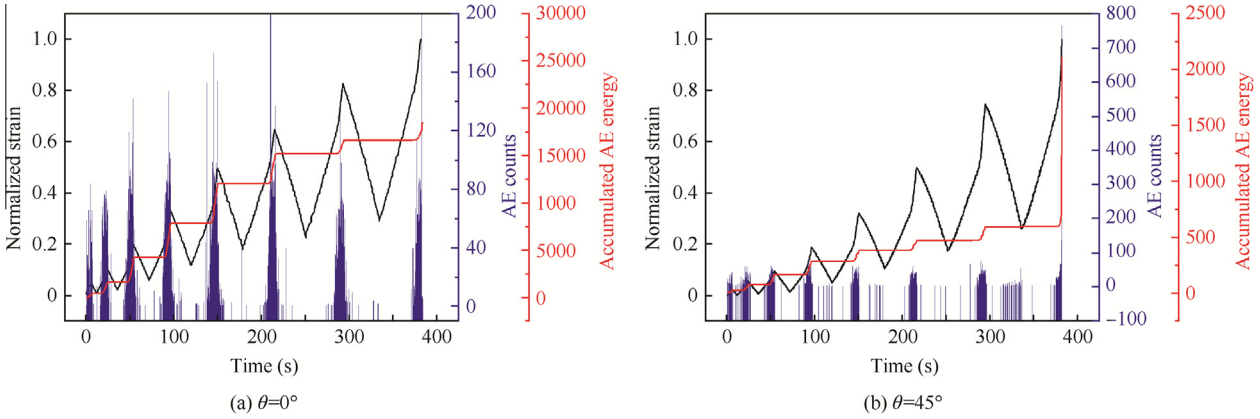

Fig. 11 Typical AE data and normalized longitudinal strain of the on- and off-axis specimens during incremental cyclic tension loadings.

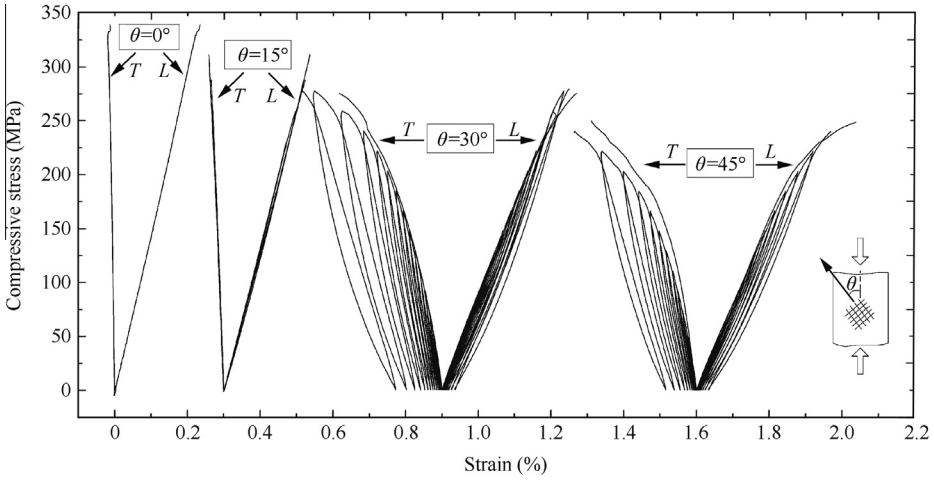

Fig. 12 Typical stress/strain curves in the GCS of the off-axis specimens with different off-axis angles (θ) under monotonic and incremental cyclic compression loadings.

tendency in initial Poisson's ratio and fracture strain as the off-axis angle θ increases, i.e., the axial anisotropy is still observable. On the other hand, the comparison results reveal the remarkable unilateral behavior of the material, since the compression specimen with the same θ shows higher proportional limit stress and strength and yet lower ultimate damage value and fracture strain along the loading direction.

The typical incremental cyclic stress/strain curves in the MCS of these off-axis specimens are shown in Fig. 13, from which one can find 'abnormal' configurations of the direct stress/strain curves in Fig. 13(a) and (b). As the compressive stress component increases, the corresponding compressive strain slows down its increasing rate beyond the elastic domain and even turns to positive values in the σ_2/ε_2 curve with remarkable 'tensile' residual strain (see Fig. 13(b)). These phenomena are probably caused by the coupling effect among strain components in the GCS. In Eq. (1), there are equations: $\varepsilon_1 = m^2\varepsilon_x + n^2\varepsilon_y + mn\gamma_{xy}$ and $\varepsilon_2 = n^2\varepsilon_x + m^2\varepsilon_y - mn\gamma_{xy}$. Under off-axis compression loadings, the strain components ε_y and γ_{xy} in the GCS keep positive, hence the related terms have inverse effects on strain ε_1. The variation of (residual) strain ε_2, however, is primarily caused by the positive term $m^2\varepsilon_y$. Since there is no obvious modulus change at low stress levels of these unloading–reloading curves, it is reasonable to assume that the compression stress components σ_1 and σ_2 do not result in additional damage.

Comparatively, the shear stress/strain curves in Fig. 13(c) depict noticeable stiffness degradation and residual strain, and the hysteresis loops exhibit new characteristics when compared with the uniaxial shear test result (see Fig. 4). For each hysteresis loop, the shear damage is visible at a low stress level, and then the damaged shear modulus partly or even fully recovers as the stress increases (this is called 'damage deactivation behavior' and will be discussed in the next section). This phenomenon is mainly attributed to the increasing compact effect resulted from the corresponding compression stress components. The matrix cracks and debonded interface tend to close, and interface debonding and sliding need to overcome higher friction resistance, and consequently the shear damage growth will be partly impeded by the compression stress. In a word, the development and exhibition of shear damage are affected by the compression stress state during off-axis compression loadings.

This damage impediment effect is further proved by the comparison results shown in Fig. 14(a) and (b), which depict the typical evolution laws of the shear damage variable and inelastic strain of the 0° Iosipescu and 30° and 45° off-axis compression specimens. It should be remarked that the shear damage of the off-axis compression specimens in Fig. 14(a) was determined still using the method illustrated in Fig. 6, and thus it would take into account the influence of the damage deactivation effect and underestimate the damage value to some extent; besides, the related results of the 15° off-axis specimens were not analyzed due to their low shear damage levels. It can be observed that these off-axis compression specimens show lower damage growth rates and critical shear damage

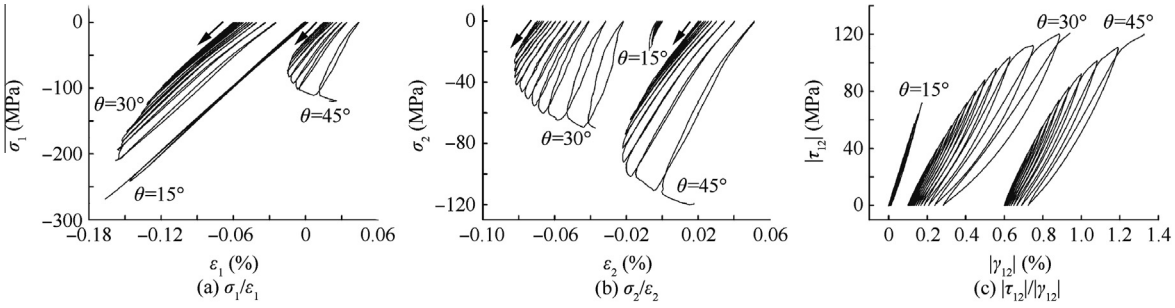

Fig. 13 Typical incremental cyclic stress/strain curves in the MCS of the off-axis compression specimens.

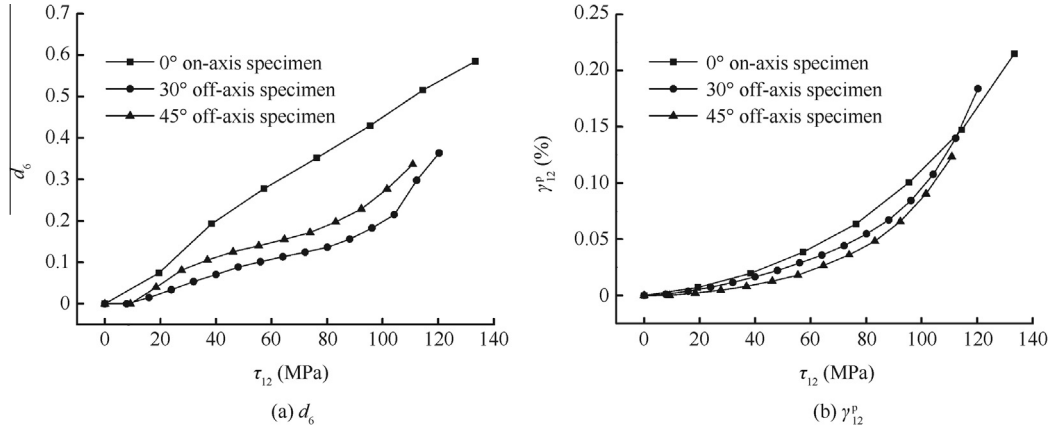

Fig. 14 Developments of damage and inelastic shear strain of the 0° Iosipescu and off-axis compression specimens as a function of τ_{12} in the MCS.

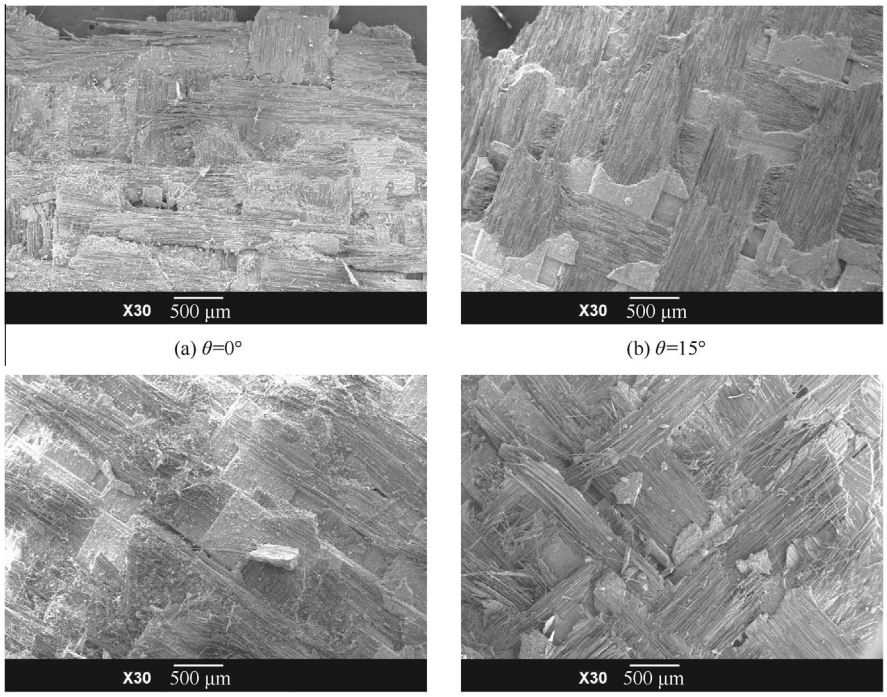

Fig. 15 SEM observations on fracture surfaces of the on- and off-axis compression specimens (the loading direction is approximately vertical).

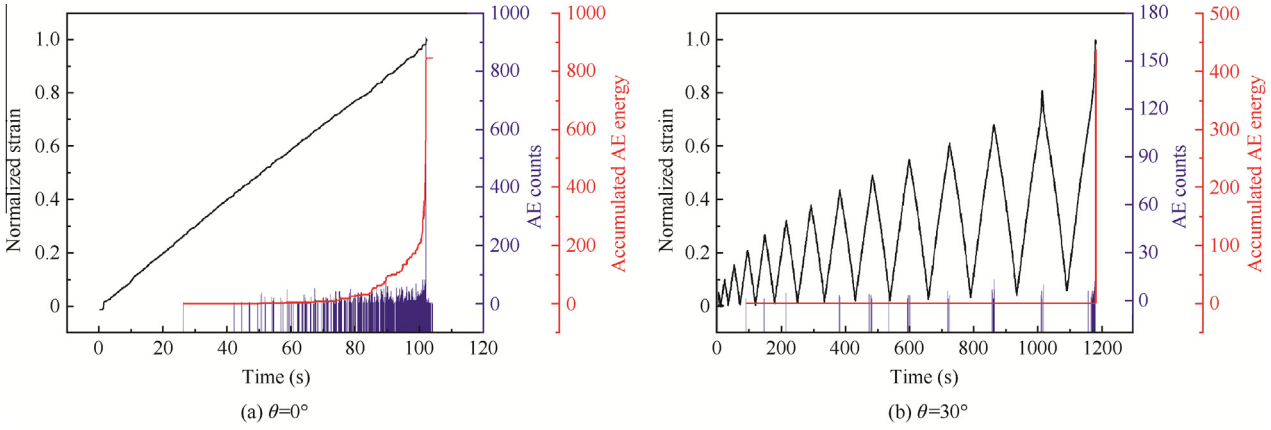

Fig. 16 Typical AE data and normalized longitudinal strain of the on- and off-axis compression specimens.

variables than those of the 0° Iosipescu shear specimens. In addition, Fig. 14(b) shows that the inelastic shear strains of these specimens exhibit a similar parabola-growth law as the corresponding stresses increase; however, less inelastic shear strain is developed in the off-axis compression specimens during most of the loading process.

SEM observations were also conducted on fracture surfaces of these compression specimens and the results are shown in Fig. 15. The typical damage and fracture modes of the 0° compression specimens (see Fig. 15(a)) including bend and shear fracture of longitudinal bundles, transverse bundle cracking and delamination can also be found in Fig. 15(b)–(d). However, the fracture surfaces of the off-axis compression specimens, especially the 30° and 45° ones, show more loosened fiber bundles. This reveals that the shear stress component does induce in-plane shear damage such as interface debonding in the fiber bundles under the combined compression and shear stress state, which could also account for the non-linear global stress/strain response (see Fig. 12) and lower mechanical strength of the off-axis compression specimens.

The typical AE data and longitudinal strain of the 0° and 30° off-axis compression specimens are shown in Fig. 16. Unlike the AE activity of the tension specimens observed in Fig. 11, most of the AE counts occur near the rupture of these compression specimens, and the total accumulated AE energy is much less than that of the tension specimens. These results accord well with the macroscopic mechanical responses in Fig. 12 that the nonlinearity of the compressive stress/strain

curves is much less remarkable than that of the tensile ones shown in Fig. 3. The fiber breakage, transverse bundle cracking and delamination observed in Fig. 15(a) should be the main AE sources of the 0° compression specimens. Comparatively, since more interface debonding and delamination were caused by the shear stress in the 30° off-axis specimen (see Fig. 15(c)), Fig. 16(b) shows that the corresponding AE energy accumulated in this specimen is lower. Besides, the "Kaiser effect" can be still observed.

3.3. Damage deactivation behavior

When the stress state changes from tension to compression, the matrix cracks formed in the loading history tend to close, which would lead to partial or even full stiffness recovery of the material. This is referred to as the "damage deactivation" process[21,30,31] and has already been verified for the 2D C/SiC composite through on-axis tension–compression tests.[4,21] In this section, we are concerned with the mechanical behaviors of the 2D C/SiC off-axis specimens under tension–compression loadings, and their comparison with the mechanical responses of the on-axis specimens.

Fig. 17 presents the representative stress/strain curves in the GCS of the 0°, 30°, and 45° off-axis specimens under tension–compression loadings. In the tension range, the non-linear stress/strain relationships are consistent with the tension test results shown in Fig. 3. After the load reversal, the longitudinal stiffness of the on-axis specimen gradually recovers as the compression increases (see Fig. 17(a)), meanwhile, the hysteresis loops approximately intersect at $O'(\sigma_r,\varepsilon_r)$, and σ_r and ε_r are generally considered to be the thermal residual stress and strain in the as-received material, respectively.[4] The stiffness recovery process can also be observed in the results of the 30° and 45° off-axis specimens (Fig. 17(b) and (c)); however, they show apparently faster deactivation rates as the compression stress σ_x increases.

Fig. 18 further presents the stress/strain curves in the MCS of the 30° and 45° off-axis specimens under tension–compression loadings. Still, the non-linear stress/strain relationships during longitudinal tension ($\sigma_1 > 0$, $\sigma_2 > 0$, and $\tau_{12} < 0$) are consistent with the off-axis tension test results shown in Fig. 5. After the longitudinal stress σ_x changes to compression ($\sigma_1 < 0$, $\sigma_2 < 0$, and $\tau_{12} > 0$), the material moduli in the MCS progressively recover to the intact state, meanwhile, continuous stress/strain relationships are maintained. Compared with the tension–compression response of the on-axis specimen (see Fig. 17(a)), Fig. 18(a) and (b) show that the off-axis compression specimens exhibit apparently faster damage deactivation rates on the principle axes of the material. Similarly, the shear stress/strain curves in Fig. 18(c) depict different mechanical responses under the off-axis tension and compression loads. During the compression loading ($\tau_{12} > 0$), the shear damage is also gradually deactivated, meanwhile, the hysteresis effect of the unloading–reloading curves becomes more evident with increasingly wider hysteresis loops overlapping each other.

It is determined that the damage deactivation rate is dependent on the compression stress state. Under on-axis and off-axis compression loadings, the damaged woven fabrics are respectively subjected to uniaxial and biaxial compression stress states according to Eq. (2), which are illustrated in Fig. 19. Under uniaxial compression loading (we suppose $\sigma_1 < 0$), the existing microscopic damages such as transverse matrix cracks in the warp and the debonded interface in the

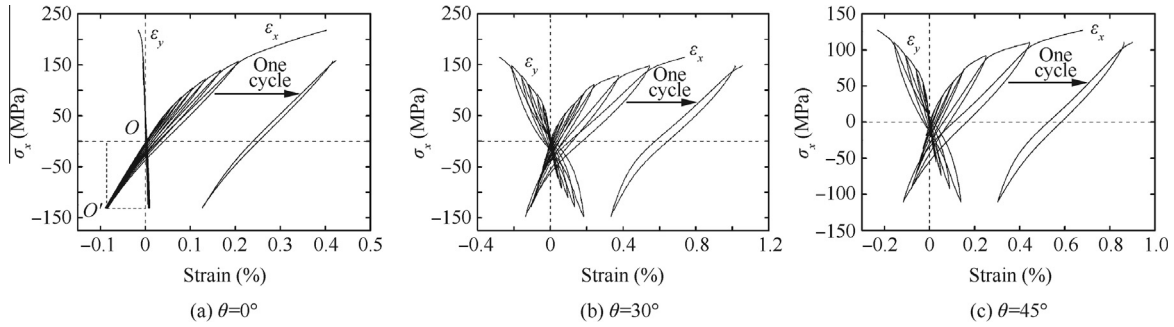

Fig. 17 Typical stress/strain curves of the specimens with different off-axis angles (θ) under tension–compression loadings.

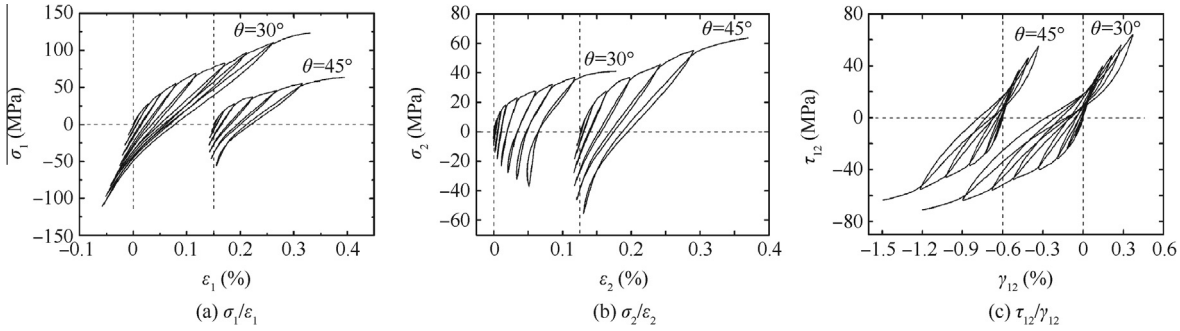

Fig. 18 Typical stress/strain curves of the 30° and 45° off-axis specimens in the MCS under tension–compression loadings.

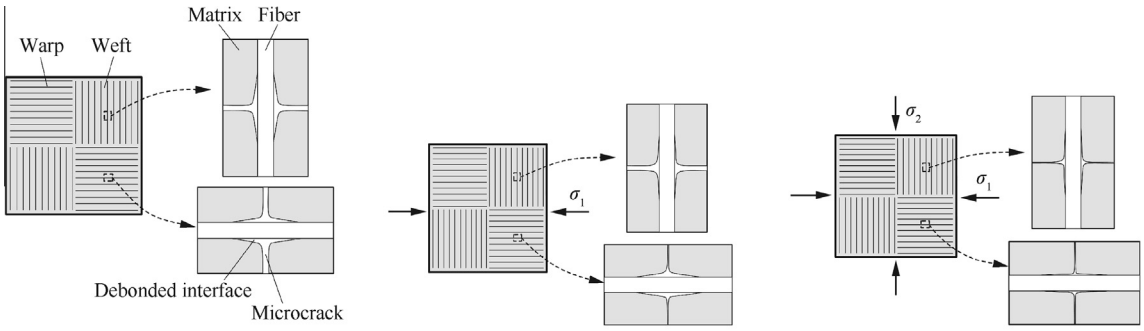

Fig. 19 A schematic of damage deactivation mechanisms of the 2D C/SiC composite under different compression stress states.

weft (see Fig. 19(a)) tend to close, which would respectively restore the load-bearing capacity of the matrix and the load-transfer ability of the interface. In this condition, the closure of matrix cracks in the warp should be the main reason for stiffness recovery along the compression direction. Comparatively, for the damaged woven fabrics subjected to biaxial compression loadings (see Fig. 19(c)), there are some differences in the damage deactivation mechanisms. In the warp, for example, the debonded interface will be driven to close by the transverse compression stress σ_2 in addition to the closure of matrix cracks caused by the longitudinal compression stress σ_1. A similar process will occur in the weft bundles. Consequently, one can deduce that the extra closure process of the debonded interface plays an important role in stiffness recovery by restoring the load-transfer capacity of the interface under biaxial compression loadings, and therefore it leads to faster damage deactivation rates in the off-axis compression specimens. This also indicates that interface debonding is one of the main damage mechanisms of the material.

4. Conclusions

(1) Mechanical behaviors of the 2D woven C/SiC composite under on-axis and off-axis loading conditions were extensively investigated through experiment and analysis. Multiple damage mechanisms were observed under tension and/or shear loadings, which resulted in the evolution of stiffness degradation and inelastic strain and the resultant non-linear stress/strain relationships of the material.

(2) The mechanical responses of the material show remarkable dependence on the loading state. Axial anisotropy is found in both tension and compression test results. The evolution rate of damage and inelastic strain is accelerated under biaxial tension and shear stress states due to the coupling effects among the damage modes. Contrarily, the compression stress partially impedes the development of shear damage under combined compression and shear loads, and moreover, it deactivates the damage during cyclic tension–compression loadings. As a result, remarkable unilateral and damage deactivation behaviors were observed in the test results of on- and off-axis specimens, and the biaxial compression stress state was found to engender a faster damage deactivation rate than the uniaxial compression case.

(3) The microscopic damage modes of the tension, shear, and compression specimens with different off-axis angles were observed by SEM, and it is found that the microscopic damage is mainly orthotropic in the material under tension and/or shear loads. AE activity is very intense in the tension specimens and it also reveals the quasi-brittle failure of the 0° compression specimen. The specimens with larger off-axis angles produce less AE energy because more damage modes with low energy levels such as interface debonding were caused by the shear stress component. The Kaiser effect was also found in this material.

(4) Based on these test results, some factors such as the evolution of damage and inelastic strain, the damage coupling effect, and the progressive damage deactivation process should be considered in order to develop an appropriate constitutive model for this material.[32]

Acknowledgements

The authors would like to acknowledge the National Key Laboratory of Thermostructure Composite Materials for providing the specimens and the financial support from the Basic Research Foundation of Northwestern Polytechnical University of China (No. JC20110219).

References

1. Nalsian R. Design, preparation and properties of non-oxide CMCs for application in engines and nuclear reactors: an overview. *Compos Sci Technol* 2004;**64**(2):155–70.
2. Christin F. Design, fabrication, and application of thermostructural composites (TSC) like C/C, C/SiC, and SiC/SiC composites. *Adv Eng Mater* 2002;**4**(12):903–12.
3. Shao YT, Liu M, Wang JP. Continuous detonation engine and effects of different types of nozzle on its propulsion performance. *Chin J Aeronaut* 2010;**23**(6):647–52.
4. Camus G, Guillaumat L, Baste S. Development of damage in a 2D woven C/SiC composite under mechanical loading: I. Mechanical characterization. *Compos Sci Technol* 1996;**56**(12):1363–72.
5. Mei H. Measurement and calculation of thermal residual stress in fiber reinforced ceramic matrix composites. *Compos Sci Technol* 2008;**68**(15–16):3285–92.
6. Morscher GN, Yun HM, DiCarlo JA. In-plane cracking behavior and ultimate strength for 2D woven and braided melt-infiltrated

SiC/SiC composites tensile loaded in off-axis fiber directions. *J Am Ceram Soc* 2007;**90**(10):3185–93.
7. Dalmaz A, Reynaud P, Rouby D, Fantozzi G. Damage propagation in carbon/silicon carbide composites during tensile tests under the SEM. *J Mater Sci* 1996;**31**(16):4213–9.
8. Zhang WH, Cheng LF, Liu YS, Zhang LT, Yang WB, Zhou ST. Fracture behaviors and mechanism of 2D C/SiC-BCx composite under tensile load. *Mater Sci Eng A* 2011;**530**:297–303.
9. Wang YQ, Zhang LT, Cheng LF, Mei H, Ma JQ. Characterization of tensile behavior of a two-dimensional woven carbon/silicon carbide composite fabricated by chemical vapor infiltration. *Mater Sci Eng A* 2008;**497**(1–2):295–300.
10. Wang MD, Laird C. Damage and fracture of a cross woven C/SiC composite subject to compression loading. *J Mater Sci* 1996;**31**(8):2065–9.
11. Guan GY, Jiao GQ, Zhang ZG. In-plane shear fracture characteristics of plain-woven C/SiC composite. *Mech Sci Technol* 2005;**24**(5):515–7 [Chinese].
12. Yan KF, Zhang CY, Qiao SR, Li M, Han D. Failure and strength of 2D-C/SiC composite under in-plane shear loading at elevated temperatures. *Mater Des* 2011;**32**(6):3504–8.
13. Wang HL, Zhang CY, Liu YS, Han D, Li M, Qiao SR. Temperature dependency of interlaminar shear strength of 2D-C/SiC composite. *Mater Des* 2012;**36**:172–6.
14. Rachid EB, Stephane B, Gerald C. Development of damage in a 2D woven C/SiC composite under mechanical loading: II. Ultrasonic characterization. *Compos Sci Technol* 1996;**56**:1373–82.
15. Morvan JM, Baste S. Effect of the opening/closure of microcracks on the nonlinear behavior of a 2D C–SiC composite under cyclic loading. *Int J Damage Mech* 1998;**7**(4):381–402.
16. Baste S. Inelastic behaviour of ceramic-matrix composites. *Compos Sci Technol* 2001;**61**(15):2285–97.
17. Mei H, Cheng LF. Thermal cycling response behavior of ceramic matrix composites under load and displacement constraints. *Mater Sci Eng A* 2008;**486**(1):235–40.
18. Evans AG, Zok FW. The physics and mechanics of fibre-reinforced brittle matrix composites. *J Mater Sci* 1994;**29**(15):3857–96.
19. Dassios KG, Aggelis DG, Kordatos EZ, Matikas TE. Cyclic loading of a SiC-fiber reinforced ceramic matrix composite reveals damage mechanisms and thermal residual stress state. *Compos Part A* 2013;**44**:105–13.
20. Li LB. Modeling hysteresis behavior of cross-ply C/SiC ceramic matrix composites. *Compos Part B* 2013;**53**:36–45.
21. Chaboche JL, Lesne PM, Maire JF. Continuum damage mechanics, anisotropy and damage deactivation for brittle materials like concrete and ceramic composites. *Int J Damage Mech* 1995;**4**(1):5–22.
22. Marcin L, Maire JF, Carrère N, Martin E. Development of a macroscopic damage model for woven ceramic matrix composites. *Int J Damage Mech* 2011;**20**:939–57.
23. Mei H, Cheng LF, Zhang LT, Luan XG, Zhang J. Behavior of two-dimensional C/SiC composites subjected to thermal cycling in controlled environments. *Carbon* 2006;**44**(1):121–7.
24. Jones RM. *Mechanics of composite materials*. 2nd ed. Philadelphia: Taylor & Francis; 1999.
25. Broughton WR. Shear. In: Hodgkinson JM, editor. *Mechanical testing of advanced fibre composites*. Cambridge: Woodhead Publishing Limited; 2000. p. 100–23.
26. Harris B, Habib FA, Cooke RG. Matrix cracking and the mechanical behaviour of SiC–CAS composites. *Proc R Soc Lond A* 1992;**437**:109–31.
27. Prasse T, Michel F, Mook G, Schulte K, Bauhofer W. A comparative investigation of electrical resistance and acoustic emission during cyclic loading of CFRP laminates. *Compos Sci Technol* 2001;**61**(6):831–5.
28. Kaya F. Damage assessment of oxide fibre reinforced oxide ceramic matrix composites using acoustic emission. *Ceram Int* 2007;**33**(2):279–84.
29. Rotem A, Baruch J. Determining the load-time history of fibre composite materials by acoustic emission. *J Mater Sci* 1974;**9**(11):1789–96.
30. Camus G. Modelling of the mechanical behavior and damage processes of fibrous ceramic matrix composites: application to a 2-D SiC/SiC. *Int J Solids Struct* 2000;**37**(6):919–42.
31. Chaboche JL, Maire JF. A new micromechanics based CDM model and its application to CMC's. *Aerosp Sci Technol* 2002;**6**(2):131–45.
32. Li J, Jiao GQ, Wang B, Li L, Yang CP. Damage characteristics and constitutive modeling of the 2D C/SiC composite: Part II – Material model and numerical implementation. *Chin J Aeronaut* 2014. http://dx.doi.org/10.1016/j.cja.2014.10.027.

Li Jun is a Ph.D. student in the School of Mechanics, Civil Engineering and Architecture at Northwestern Polytechnical University in China. His area of research includes continuum damage mechanics and non-linear mechanical behavior of ceramic matrix composites and structures.

Jiao Guiqiong is a professor and Ph.D. advisor in the School of Mechanics, Civil Engineering and Architecture at Northwestern Polytechnical University in China. His research interests are mechanics of composite materials including polymer matrix composites, ceramic matrix composites, short fiber reinforced plastic, and their structural applications.

Wang Bo is an associated professor in the School of Mechanics, Civil Engineering and Architecture at Northwestern Polytechnical University in China. His main research interests are mechanics of ceramic and polymer matrix composite materials and their applications.